Organic Electronics 26 (2015) 92–98

Contents lists available at ScienceDirect

Organic Electronics

journal homepage: www.elsevier.com/locate/orgel

In-plane electroluminescence from microcavity organic light-emitting transistors

Yongsheng Hu, Li Song, Dongwei Li, Jie Lin, Xingyuan Liu *

State Key Laboratory of Luminescence and Applications, Changchun Institute of Optics, Fine Mechanics and Physics, Chinese Academy of Sciences, Changchun 130033, China

ARTICLE INFO

Article history:
Received 27 April 2015
Received in revised form 5 July 2015
Accepted 6 July 2015
Available online 16 July 2015

Keywords:
Organic light-emitting transistor
In-plane
Microcavity
Distributed Bragg reflector
Charge generation
Electroluminescence

ABSTRACT

We report the observation of in-plane emission beneath the drain electrode in multilayer heterostructure organic light-emitting transistors (OLETs). A novel modification method for the interface between the hole transport layer and the emission layer has been proposed, which brought a great enhancement for the light power and external quantum efficiency. Further, distributed Bragg reflector was incorporated to the in-plane-emitted OLETs, which combined with the top thin layer of Au, forming a vertical microcavity. The electroluminescence spectra were significantly altered by the microcavity and much narrower linewidth was obtained. The results will help to develop high color purity and white OLETs with high performance, which would be useful for multifunctional displays.

© 2015 Elsevier B.V. All rights reserved.

1. Introduction

Organic light-emitting transistors (OLETs) are a novel kind of multifunctional optoelectronic devices which combined the electroluminescence (EL) characteristic of organic light-emitting diodes (OLEDs) and the switching characteristic of organic field-effect transistors [1,2]. The multifunctional property ensures them wide applications such as flat panel displays and optical communication systems, since much simpler process and higher degree of integration could be achieved [3,4].

In an OLET, the location of the emission zone is greatly determined by the device structure and the relative transportation ability between holes and electrons. Generally, the emission zone lies within the channel and presents as a line-shape with a width between 2 and 10 μm [5,6]. The location and width of the emission zone is usually gate voltage (V_{GS}) depended for devices with ambipolar characteristic. For OLETs with unipolar characteristic, the emission zone is likely to be restricted to the vicinity of the electrode where the minority carriers are injected [4,7]. Recently, Toffanin et al. observed in-plane emission both in the channel and beneath the electrode in trilayer heterostructure OLETs, which overcomes the long-existed drawback of line-shaped emission which restricts the aperture ratio for OLETs-based displays [6,8]. Ullah et al. achieved an intense in-plane emission beneath the electrode in double layer heterostructure OLETs by utilizing a non-planar asymmetrical electrodes technology [3]. The device also presented impressive performance which manifests the advantages of heterostructure OLETs for the use of displays.

Nevertheless, when incorporating carrier transport layer with high carrier mobility and emission layer (EML) with high photoluminescence efficiency simultaneously, there would probably be energy-misalignment and thus great carrier injection barriers are formed between the two layers, which would result in low efficiency for exciton formation and finally restrict the further promotion for the performance of the devices [9–11]. Interfacial modification is an effective way to minimize the injection barriers. However, large amount of studies have been focused on the interfaces of the electrode/organic layer and the insulator/organic layer [10,12–14]. To the best of our knowledge, there is little report on the interface modification between organic/organic layers in OLETs. Transition metal oxide, i.e. MoO_x, is a common kind of modification layer, which is used between the electrode and organic layer to promote the hole injection [7,15]. In our work, we tried to incorporate MoO_x between the organic layers, and found that it brought a great enhancement for the emissive characteristic of the devices.

Microcavity formed by distributed Bragg reflector (DBR)/DBR or DBR/metal reflectors is able to manipulate the distribution of optical field in the cavity. It has played an important role in the application of adjusting the EL properties of OLEDs and providing an optical resonator for organic lasers [16–19]. Namdas et al. has

* Corresponding author.
E-mail address: liuxy@ciomp.ac.cn (X. Liu).

http://dx.doi.org/10.1016/j.orgel.2015.07.015
1566-1199/© 2015 Elsevier B.V. All rights reserved.

observed enhanced performance of OLETs by using DBR as the bottom reflector, which was composed of 3 pairs of SiN_x/SiO_2 [20]. However, as the insulator layer simultaneously, the DBR used had only a limited pairs and a low reflectance. In addition, one DBR could not make an effective microcavity structure that ideal cavity effect required.

In this work, we report the observation of in-plane EL emission beneath the drain electrode in multilayer heterostructure OLETs. Ultra-thin MoO_x layer was used to modify the interface between the hole transport layer (HTL) and the EML, which brought a great enhancement for the light power and external quantum efficiency (EQE). By incorporating high reflective bottom DBR, we constructed microcavity OLETs with in-plane narrow band light emission due to microcavity effect. The results are beneficial to the development of high color purity and white OLETs with high performance for multifunctional displays.

2. Experimental details

2.1. Materials and device preparation

Pentacene, CBP, $Ir(piq)_2acac$ and TPBI were purchased from Lumtech. PTCDI-C13, polystyrene (PS), Poly-4-vinylpenol (PVP) and MoO_x were purchased from Sigma–Aldrich. 66 nm TiO_2, 106 nm SiO_2 and 78 nm ITO were deposited onto the glass substrate by e-beam evaporation under a base pressure of 1.5×10^{-4} Pa, evaporation rate of 2 Å/s, and substrate temperature of 300 °C. An end-Hall ion source was used to assist the deposition. PVP and PS were spun coated in the way reported elsewhere [21]. Pentacene, MoO_x, CBP:$Ir(piq)_2acac$ (~6 Wt%), TPBI and PTCDI-C13 were successively thermal evaporated with the rate of 0.2, 0.05, 2, 0.2 and 0.5 Å/s, respectively. Au was evaporated on top of PTCDI-C13 through a shadow mask with channel length and width of 60 μm and 3000 μm, respectively, which acted as the source and drain electrodes. The substrate was kept at room temperature during the deposition process. The devices were encapsulated with UV glue in the glovebox (H_2O, O_2 <0.1 ppm) before testing.

2.2. Characterization

The electrical characteristics were performed by Keithley 4200 SCS at room temperature under air ambient. The photocurrent was recorded by HAMAMATSU S1336 photodiode. The channel images were captured by Olympus BX51TRF CCD microscope with a 20× objective lens. The EL spectra were recorded by AvaSpec-ULS2048L fiber spectrometer. The absorption spectra were recorded by Shimadzu UV-3101PC UV–vis–NIR spectrophotometer. The carrier mobilities were calculated by the formula for the saturation regime: $I_{DS} = \mu C_i(W/2L)(V_{GS} - V_T)^2$, (where μ is the field-effect mobility, C_i is the gate dielectric capacitance density, V_T is the threshold voltage, V_{GS} is the gate-source voltage, and W and L are the channel width and length, respectively). The EQE was calculated as follows:

$$\mathrm{EQE} = \frac{P_{tot}/E_{ph}}{I/q} = \frac{P_{tot}(W)}{I(A)E_{ph}(\mathrm{eV})} = \frac{I_{ph}/K(A/W)}{I_{DS}E_{ph}(\mathrm{eV})} \approx 1.5\frac{I_{ph}}{I_{DS}} \quad (1)$$

where P_{tot}, K, E_{ph}, I_{ph}, I_{DS} and q are the total emitted light power, photo sensitivity of the detector (0.3 A/W), average photon energy, photocurrent, drain current and electron charge, respectively.

3. Results and discussion

Fig. 1 shows the schematic of the device, the energy levels of the materials and the molecular structures. Organic semiconductors with high carrier mobility rather than a matched energy level are our priorities to choose materials. Pentacene and PTCDI-C13 were therefore used as the HTL and the electron transport layer (ETL), respectively, since they have shown good ambipolar transportation characteristic [22]. Highly efficient phosphorescent donor–acceptor system CBP:$Ir(piq)_2acac$ was used as the EML. TPBI is a widely used ETL and hole block layer in OLEDs [23,24]. Since the LUMO level of TPBI lies between that of CBP and PTCDI-C13, it can lower the electron injection barrier between ETL and EML as a secondary ETL. According to Fig. 1(b), there is large hole injection barrier between pentacene and CBP, which will result in low efficiency for hole injection and exciton formation. Considering that MoO_x is able to function as a charge generation layer between the two subunits of a tandem OLED [25], we attempted to introduce it as a modification layer at the interface of HTL/EML, expecting for an enhancement for the performance of the devices.

We first investigated the influence of the thickness of MoO_x. Devices with different thicknesses of MoO_x were fabricated: Glass/ITO/PVP(420 nm)/PS(30 nm)/pentacene(48 nm)/MoO_x(0 nm, 0.15 nm, 0.25 nm, 0.5 nm)/CBP:$Ir(piq)_2acac$(24 nm)/TPBI(14 nm)/PTCDI-C13(30 nm)/Au(15 nm). We observed the light emission from the top of the devices.

Fig. 2(a) shows the transfer characteristics ($V_{DS} = -100$ V) for different devices. For device without MoO_x, ambipolar characteristic is observed, which is resulted from the carrier transport layer material system we chose. The hole and electron mobilities are $0.04\ cm^2\ V^{-1}\ s^{-1}$ and $0.0014\ cm^2\ V^{-1}\ s^{-1}$, respectively. Fig. 2(b) and (c) show the corresponding photocurrent (I_{ph}) and EQE. The I_{ph} gets a maximum around $V_{GS} = -40$ V. The EQE also reaches to the maximum of 0.007% at this regime, where the device is under ambipolar operation. The well-balanced transportation of carriers at this regime is attributed to the maximum EQE. For device with 0.15 nm MoO_x, it can be seen from Fig. 2(a), the drain current (I_{DS}) increases significantly at the hole accumulation regime ($V_{GS} = -80$ V ~ -120 V), which indicates that the hole concentration is greatly increased. On the other hand, the I_{DS} is partly restricted at the electron accumulation regime ($V_{GS} = 0$ V ~ 20 V). The I_{ph} generally increases as the V_{GS} increases and reaches to 20 nA at $V_{GS} = -120$ V, which is approx. 50 times higher than that without MoO_x. The EQE reaches to 0.01%, which is also promoted compared to that without MoO_x. As MoO_x grows to 0.25 nm, the I_{DS} continues to increase, which indicates the continuous increase of hole concentration. At the regime of $V_{GS} = 0$ V ~ 20 V, the I_{DS} is around 40 μA, which is approx. one order of magnitude higher than that without MoO_x. This implies that the I_{DS} at this regime is probably resulted from the carriers generated by MoO_x. We will stress this point later. As for the I_{ph} and EQE, there is further improvement compared to that with 0.15 nm MoO_x. The maximum I_{ph} and EQE reach to 87 nA and 0.03%, respectively, and the EQE maintains at 0.015% even for high V_{GS} (which means high current density). Although the EQE is lower than state-of-the-art for heterojunction OLETs [3,6], there is several orders of magnitude enhancement for devices based on pentacene and PTCDI-C13 [26,27]. As MoO_x increases to 0.5 nm, the I_{DS} still continues to increase, while the on/off ratio decreases greatly. This implies that MoO_x would generate more carriers, which beyond the modulation by the potential difference between the gate electrode and an opposite electrode [28]. However, the increasing of I_{ph} is slowing down, and even lower than that with 0.25 nm MoO_x at high V_{GS}. The EQE is also smaller than that with 0.25 nm MoO_x, which is probably related to the unbalanced carrier transportation and charge induced quenching of excitons due to the excess holes. Fig. 2(d) presents the output characteristic of device with 0.25 nm MoO_x, which owns the best EQE of the four devices. It is shown that the device exhibits unipolar operation characteristic.

We also observed the characteristic of emission zones for the four devices under different V_{GS}. Fig. 3 presents the images of the

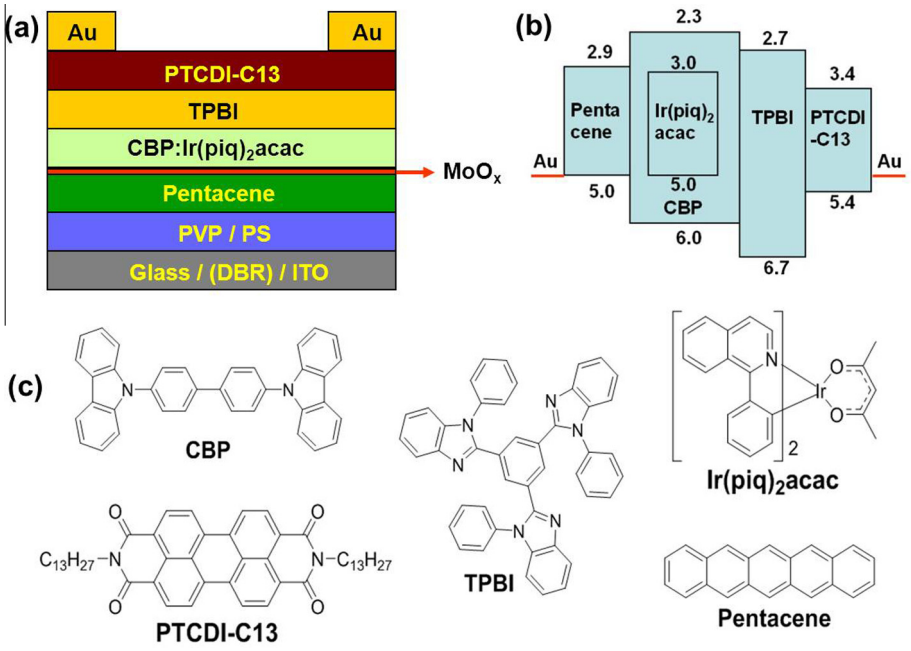

Fig. 1. (a) Schematic of the device; (b) energy levels of the materials; (c) molecular structures.

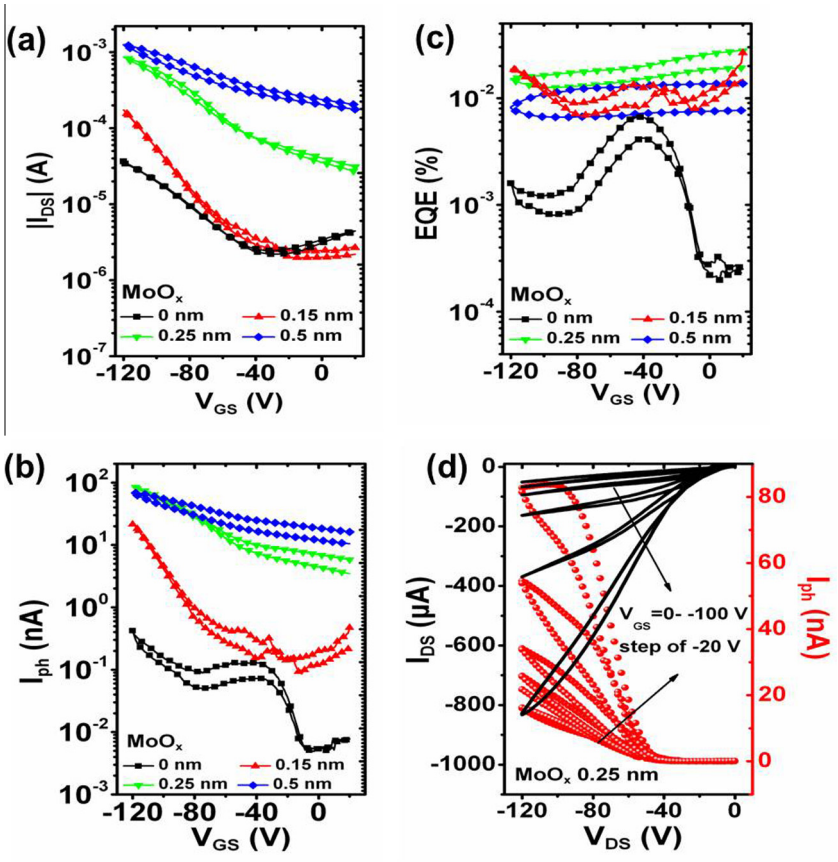

Fig. 2. Characteristics for devices with different thickness of MoO_x: (a) transfer curves at $V_{DS} = -100$ V; (b) the corresponding I_{ph}; (c) the corresponding EQE; (d) output curve and the corresponding I_{ph} for device with 0.25 nm MoO_x.

emission zones. In consideration of the great differences of the emission intensity for the four devices, to better observe the change of the emission zones, we use different exposure times when capture the images, as explained in the figure caption. It can be seen from Fig. 3(a) that the emission zone locates beneath the drain electrode for device without MoO_x. The emission zone extends from the side of the drain electrode close to the channel to the other side as the V_{GS} increases from −40 V to −120 V. For

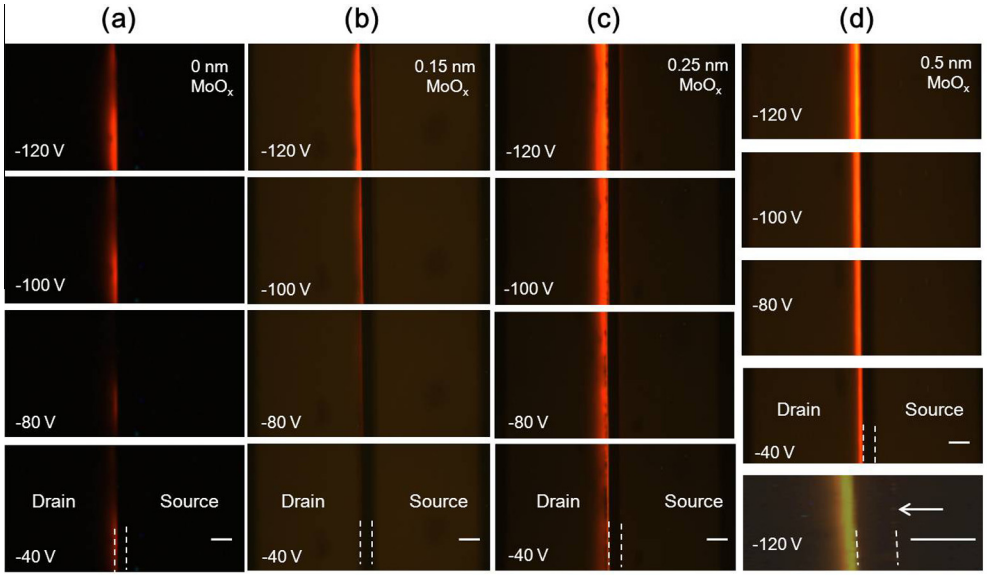

Fig. 3. Optical images of the emission zones for devices with different thickness of MoO_x under different V_{GS} (V_{DS} is fixed at −100 V while V_{GS} is −120 V, −100 V, −80 V and −40 V from the top to the bottom, respectively: (a) MoO_x is 0 nm; (b) MoO_x is 0.15 nm; (c) MoO_x is 0.25 nm; (d) MoO_x is 0.5 nm. The exposure time is 4 s for (a) and the last sub image of (d) (V_{GS} = −120 V), and 1 s for the remaining images. The arrow in the last sub image of (d) shows the location of the emission zone at the source electrode. All the scale bars denote 100 μm.

device with 0.15 nm MoO_x, in addition to the emission zone beneath the drain electrode, there is a new emission zone at the edge of source electrode near the channel (V_{GS} = −120 V). The new emission zone appears as line-shaped, and the intensity is much weaker than the one beneath the drain electrode. The intensity of the two emission zones are both weakened as the V_{GS} decreases. For device with 0.25 nm MoO_x, the two emission zones still exist and their widths have increased. The width of the emission zone beneath the drain electrode reaches to ~75 um when V_{GS} = −120 V. For device with 0.5 nm MoO_x, the emission zone beneath the drain electrode still exists, however, the one at the source electrode is almost disappeared. By observing under lower background light noise and longer exposure time, it is still can be seen (the last sub image of Fig. 3(d). Given to the change of the emission zone at the source electrode, we suggest that it is resulted from the introduction of MoO_x, and an optimized thickness of MoO_x will bring considerable enhancement for the emission zone beneath the drain electrode.

The schematic of the carrier injection and transport of devices with MoO_x is shown in Fig. 4(b) based on the above experimental observations. According to Tang's study, in tandem OLEDs where MoO_x functions as an interconnect layer between the two subunits, spontaneous electron transfer occurs in a vacuum-deposited MoO_x layer from various defect states to the conduction band via thermal diffusion [29]. The external electric-field induces the charge separation through tunneling of generated holes and electrons from MoO_x into the neighboring HTL and ETL, respectively [29]. Similarly, we assume that there are charges generated in the MoO_x layer for our devices. To confirm this, we measured the UV–vis–NIR absorption spectra for pentacene film, MoO_x film and MoO_x doped pentacene film, as is shown in Fig. 4(a). The newly emerged absorption peak at around 930 nm corresponds to the electron transfer state formed between MoO_x and pentacene [30–32]. When the devices are operating in the hole accumulation mode, the MoO_x near the source electrode will suffer from forward voltage bias in the vertical direction. Assisted by the strong electric field, the generated holes can be injected from MoO_x to the HOMO level of pentacene, which is probably the main reason for the enhancement of I_{DS}. There is a large possibility of injection of the generated electrons from MoO_x into the EML. The generated holes, together with the accumulated holes in pentacene, will transport towards the drain electrode, and recombine with the electrons injected from the drain electrode in the EML, which results for the intense emission beneath the drain electrode. The generated electrons may inject to the EML and recombine with part of the holes injected from the source electrode and results for the emission at the source electrode. The weaker intensity is possibly due to the large energy gap between the defect levels of MoO_x and CBP's LUMO level. Admittedly, we cannot rule out the following possibility with regard to the emission at the source electrode. Electrons in the ETL transport to the vicinity of source electrode and then inject to the EML by the attraction of the large amount of holes under the source electrode and finally recombine with the holes in the EML. This possible recombination route is not depicted in Fig. 4(b), and further research work is needed to confirm the origin of the emission.

Considering that the emission area locates beneath the Au electrode, which could act as a mirror since it is partly reflected, it would be convenient to construct a vertical microcavity by only incorporating DBR as the bottom mirror with high reflectance. DBRs were fabricated by depositing 15 pairs of TiO_2/SiO_2 together with a thin layer of ITO, which also functions as the gate electrode. The central wavelength (λ_0) was 618 nm. Since $d = \lambda_0/4n$ (where d and n are the physical thickness and refractive index, respectively, for each layer), the physical thicknesses for TiO_2, SiO_2 and ITO were 66 nm, 106 nm and 78 nm, respectively. The detailed structures of the devices are as follows: Glass/DBR/ITO/PVP(420 nm)/PS(30 nm)/pentacene(48 nm)/MoO_x(0.25 nm)/CBP:Ir(piq)$_2$acac(24 nm)/TPBI (14 nm)/PTCDI-C13(30 nm)/Au(15 nm, 30 nm). Fig. 5(a)–(b) present the transfer curves and the corresponding I_{ph} and EQE of the two devices. The thickness of Au brings little impact to I_{DS}, however, with great impact to I_{ph}. The I_{ph} for device with 30 nm Au is only half to that with 15 nm Au, which is mainly due to the greater absorption of Au, since the emission zones still maintain well beneath the drain electrode (insets of Fig. 5(c) and (d). The lower I_{ph} causes the lower EQE. Fig. 5(c) and (d) show the EL spectrums of the two devices and that for device without DBR. It is a typical EL spectrum from CBP:Ir(piq)$_2$acac, where the main peak lies at

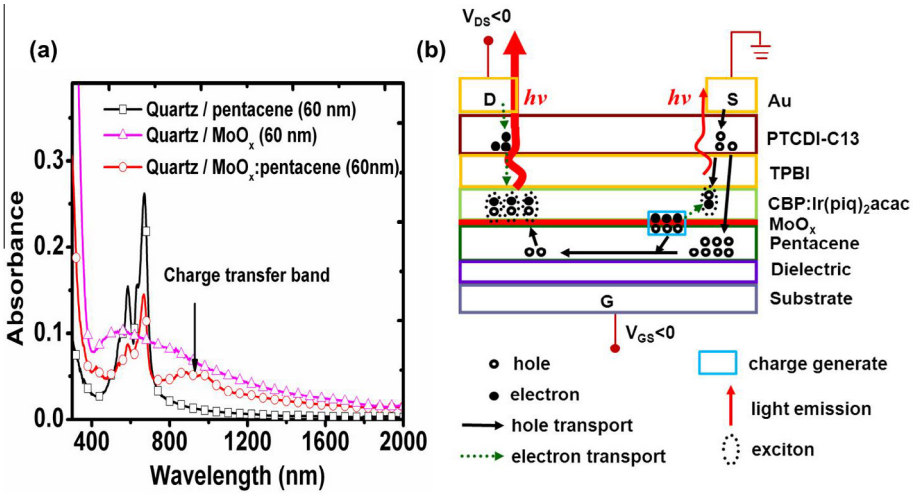

Fig. 4. (a) UV–vis–NIR absorption spectra of a pentacene film (60 nm), a MoO_x film (60 nm), and a MoO_x-doped pentacene film (60 nm, 50% mol MoO_x); (b) schematic of the carrier injection and transport.

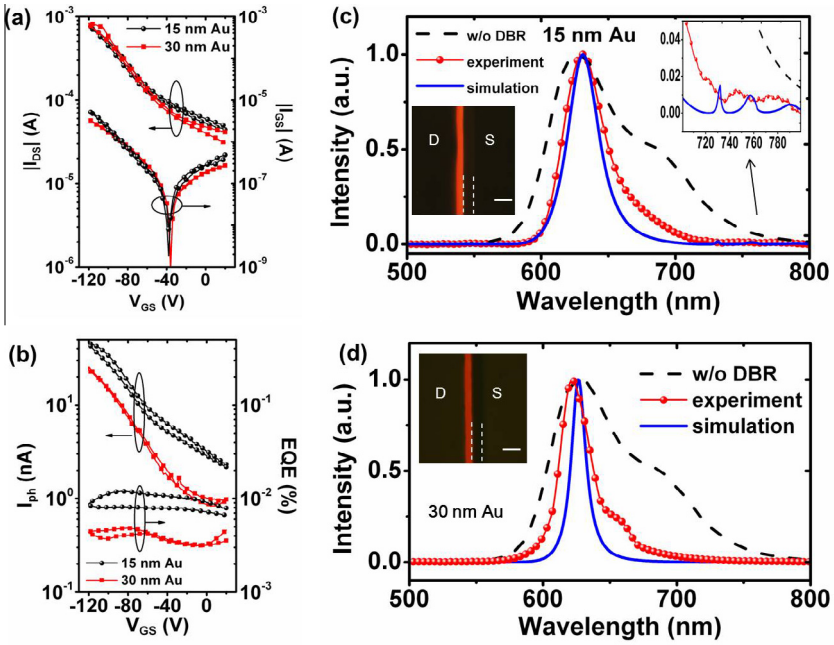

Fig. 5. (a) Transfer curves and the corresponding gate current for the microcavity devices; (b) the corresponding I_{ph} and EQE; (c) the experimental (V_{GS} = −120, V_{DS} = −100 V) and the simulated EL spectra for the device with 15 nm Au, the inset is the optical image of the emission zone and the partial enlarged drawing of the spectrum, respectively; (d) the experimental (V_{GS} = −120, V_{DS} = −100 V) and the simulated EL spectra for the device with 30 nm Au, the inset is the optical image of the emission zone.

627 nm and a shoulder peak near 700 nm, for device without DBR. The linewidth (full width half magnitude, FWHM) for the spectrum is 88 nm. There are great changes of the EL spectra for devices combining DBR. For device with 15 nm Au, the main peak red shifts to 631 nm and the FWHM reduces to 35 nm. For devices with 30 nm Au, the main peak blue shifts to 622 nm and the FWHM reduces to only 26 nm. The changes in the EL spectra originate from the microcavity effect. We also calculated the EL spectra for microcavity devices by [33,34]:

$$|E_c(\lambda)|^2 = \frac{(1-R_L)[1+R_H+2\sqrt{R_H}\cos(-\phi_H+4\pi n_{org}z_0/\lambda)]}{(1-R_HR_L)^2+4\sqrt{R_HR_L}\sin^2(\Delta\phi/2)}|E_c(\lambda)|^2 \quad (2)$$

$$\Delta\phi = -\phi_H-\phi_L+\sum_i 4\pi n_i d_i/\lambda \quad (3)$$

with the resonance condition: $\Delta\phi = 2\pi m$ (m = 0,1,2…), in which R_H and R_L are the reflectance of Glass/DBR/ITO and Au, respectively; z_0 is the physical distance from ITO to the exciton radiative recombination zone, which is supposed to be at the interface of CBP/TPBI; n_i and d_i are the refractive index and physical thickness, respectively, for the materials between ITO and Au; $|E_n(\lambda)|^2$ is the EL spectrum in the free space; ϕ_H and ϕ_L are the phase shifts for Glass/DBR/ITO and Au, respectively, which can be calculated using the characteristic matrix of each layer [35]. The parameters required for the calculation are listed in Table 1. The calculated EL spectra for the two devices are presented in Fig. 5(c) and (d).

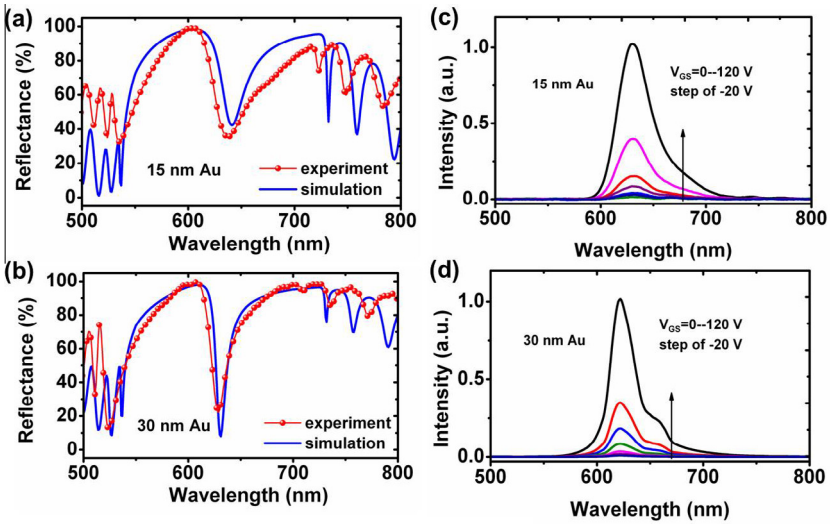

Fig. 6. Experimental and simulated reflectance from the Au side of samples (the Au covering the whole surface) with the same structure as the microcavity devices: (a) 15 nm Au; (b) 30 nm Au; The EL spectra for the microcavity devices under different V_{GS} (V_{DS} is fixed at −100 V): (c) 15 nm Au; (d) 30 nm Au.

Table 1
Thickness and refractive index of the materials.

Materials	Thickness (nm)	Index	Wavelength (nm)
Glass	10^6	1.52	500–800
TiO_2	66	2.34	
SiO_2	106	1.46	
ITO	78	2.0	
PVP	420	1.53	
PS	30	1.59	
Organic layers	116	1.75	
MoO_x	/	/	/
Au	15 or 30	0.84–i1.84	500
		0.33–i2.32	550
		0.2–i2.9	600
		0.13–i3.84	700
		0.15–i4.65	800

Compared with the experiment, the location of the emission peaks is basically the same but with narrower FWHM. The following reasons are probably responsible for the difference of the FWHM between the experiment and the simulation as well as the shoulder peak near 660 nm for device with 30 nm Au: (1) there is minor difference for the refractive index; (2) the absorption of the materials (exclude Au) is neglected; (3) a very small part of emission locates at the vicinity of the electrodes that is affected little by the microcavity effect. Nevertheless, what is certain is that the microcavity brings a great effect in adjusting and narrowing the EL spectra of the devices.

To better interpret the change of the EL spectra, we tested the reflectance from the Au side of samples with the same structure as the devices but with the Au covering the whole surface. The results are shown in Fig. 6(a) and (b). For devices with 15 nm Au, there are 4 resonant peaks in the range of 600–800 nm. The resonant peaks at 637 nm, 723 nm and 748 nm are in accordance to the EL spectra of the device (Fig. 5(c)), while the resonant peak at 784 nm does not correspond to any peak in the EL spectra, which is probably due to the low intensity of the EL spectrum of CBP:Ir(piq)$_2$acac at this region. Similarly, for sample with 30 nm Au, the resonant peak at 628 nm corresponds to the emission peak at 622 nm of the device. The calculated reflectance by the method of transfer matrix [35] is also shown in Fig. 6(a) and (b). Compared to the experiment, the number of resonant peaks is consistent, while the position of the peaks and the reflectance is slightly different, which should also be related to the minor difference in refractive index and the absorption of the materials. Fig. 6(c) and (d) are the EL spectra at different V_{GS} for the two devices. The position of emission peaks stays unchanged.

4. Conclusions

In conclusion, we have observed in-plane emission beneath the drain electrode in multilayer heterostructure OLETs, based on the structure of which, a microcavity can be very simply realized by only introducing a bottom DBR. We have proposed an effective interfacial modification method to promote the performance of the device. By inserting an ultra-thin layer of MoO_x, which functions as a charge generation layer, between the HTL and EML, the light power and EQE promotes 2 orders of magnitude and 1 order of magnitude, respectively, and the EQE maintains unchanged at high current density. The incorporating of vertical microcavity brings a great effect for adjusting and narrowing the EL spectra of the in-plane emission devices. Our results provide some insights for the optimization of OLETs with heterostructure and the manipulation of the EL spectra for better use for multifunctional displays.

Acknowledgments

This work was supported by the CAS Innovation Program, and the National Science Foundation of China through Grant Nos. 51102228, 61106057, 6140031454, and project supported by State Key Laboratory of Luminescence and Applications.

References

[1] C. Santato, F. Cicoira, R. Martel, Nat. Photonics 5 (2011) 392–393.
[2] F. Cicoira, C. Santato, Adv. Funct. Mater. 17 (2007) 3421–3434.
[3] M. Ullah, A. Armin, K. Tandy, S.D. Yambem, P.L. Burn, P. Meredith, E.B. Namdas, Sci. Rep. 5 (2015) 8818.
[4] R. Capelli, S. Toffanin, G. Generali, H. Usta, A. Facchetti, M. Muccini, Nat. Mater. 9 (2010) 496–503.
[5] M. Ullah, K. Tandy, S.D. Yambem, M. Aljada, P.L. Burn, P. Meredith, E.B. Namdas, Adv. Mater. 25 (2013) 6213–6218.
[6] S. Toffanin, R. Capelli, W. Koopman, G. Generali, S. Cavallini, A. Stefani, D. Saguatti, G. Ruani, M. Muccini, Laser Photonics Rev. 7 (2013) 1011–1019.
[7] K. Tandy, M. Ullah, P.L. Burn, P. Meredith, E.B. Namdas, Org. Electron. 14 (2013) 2953–2961.
[8] C. Soldano, A. Stefani, V. Biondo, L. Basirico, G. Turatti, G. Generali, L. Ortolani, V. Morandi, G.P. Veronese, R. Rizzoli, R. Capelli, M. Muccini, ACS Photonics 1 (2014) 1082–1088.

[9] B.B.Y. Hsu, J. Seifter, C.J. Takacs, C. Zhong, H.-R. Tseng, I.D.W. Samuel, E.B. Namdas, G.C. Bazan, H. Fei, Y. Cao, A.J. Heeger, ACS Nano 7 (2013) 2344–2351.
[10] J.H. Seo, E.B. Namdas, A. Gutacker, A.J. Heeger, G.C. Bazan, Appl. Phys. Lett. 97 (2010) 043303.
[11] C.A. Di, G. Yu, Y.Q. Liu, X.J. Xu, D.C. Wei, Y.B. Song, Y.M. Sun, Y. Wang, D.B. Zhu, Adv. Funct. Mater. 17 (2007) 1567–1573.
[12] M.C. Gwinner, Y. Vaynzof, K.K. Banger, P.K.H. Ho, R.H. Friend, H. Sirringhaus, Adv. Funct. Mater. 20 (2010) 3457–3465.
[13] O. Acton, M. Dubey, T. Weidner, K.M. O'Malley, T.W. Kim, G.G. Ting, D. Hutchins, J.E. Baio, T.C. Lovejoy, A.H. Gage, D.G. Castner, H. Ma, A.K.Y. Jen, Adv. Funct. Mater. 21 (2011) 1476–1488.
[14] X.N. Sun, C.A. Di, Y.Q. Liu, J. Mater. Chem. 20 (2010) 2599–2611.
[15] H. Nakanotani, M. Saito, H. Nakamura, C. Adachi, Appl. Phys. Lett. 95 (2009).
[16] S.J. Han, C.J. Huang, Z.H. Lu, J. Appl. Phys. 97 (2005).
[17] S. Kena-Cohen, S.R. Forrest, Nat. Photonics 4 (2010) 371–375.
[18] X.Y. Liu, H.B. Li, C.Y. Song, Y.Q. Liao, M.M. Tian, Opt. Lett. 34 (2009) 503–505.
[19] M. Thomschke, R. Nitsche, M. Furno, K. Leo, Appl. Phys. Lett. 94 (2009) 083303.
[20] E.B. Namdas, B.B. Hsu, J.D. Yuen, I.D. Samuel, A.J. Heeger, Adv. Mater. 23 (2011) 2353–2356.
[21] N. Zhang, J. Lin, J.S. Luo, Y.T. Li, Z.H. Gan, Y. Fan, X.Y. Liu, Appl. Phys. Express 7 (2014) 021601.
[22] Y.S. Hu, Q.P. Lu, H. Li, N. Zhang, X.Y. Liu, Appl. Phys. Express 6 (2013) 051602.
[23] Q.S. Zhang, B. Li, S.P. Huang, H. Nomura, H. Tanaka, C. Adachi, Nat. Photonics 8 (2014) 326–332.
[24] Z.Q. Gao, C.S. Lee, I. Bello, S.T. Lee, R.M. Chen, T.Y. Luh, J. Shi, C.W. Tang, Appl. Phys. Lett. 74 (1999) 865–867.
[25] Q.Y. Bao, J.P. Yang, Y.Q. Li, J.X. Tang, Appl. Phys. Lett. 97 (2010) 063303.
[26] C. Rost, S. Karg, W. Riess, M.A. Loi, M. Murgi, M. Muccini, Synth. Met. 146 (2004) 237–241.
[27] H.S. Seo, D.K. Kim, J.D. Oh, E.S. Shin, J.H. Choi, J. Phys. Chem. C 117 (2013) 4764–4770.
[28] K. Yamada, T. Yamao, S. Hotta, Adv. Mater. 25 (2013) 2860–2866.
[29] J.P. Yang, Y. Xiao, Y.H. Deng, S. Duhm, N. Ueno, S.T. Lee, Y.Q. Li, J.X. Tang, Adv. Funct. Mater. 22 (2012) 600–608.
[30] H. Nakanotani, M. Saito, H. Nakamura, C. Adachi, Appl. Phys. Lett. 95 (2009) 103307.
[31] T. Matsushima, Y. Kinoshita, H. Murata, Appl. Phys. Lett. 91 (2007) 253504.
[32] T. Matsushima, G.H. Jin, Y. Kanai, T. Yokota, S. Kitada, T. Kishi, H. Murata, Org. Electron. 12 (2011) 520–528.
[33] S.J. Han, C.J. Huang, Z.H. Lu, J. Appl. Phys. 97 (2005) 093102.
[34] D.G. Deppe, C. Lei, C.C. Lin, D.L. Huffaker, J. Mod. Opt. 41 (1994) 325–344.
[35] H.A. Macleod, Thin-Film Optical Filters, third ed., Institute of Physics Publishing, Bristol and Philadelphia, 2001.